Reliability and Lifetime Prediction Model of Sintered Silver under High-Temperature Cycling

Paul Paret, *Member, IEEE*, Joshua Major, *Member, IEEE*, Douglas DeVoto, *Member, IEEE*, Sreekant Narumanchi, *Senior Member, IEEE*, Chao Ding, *Member, IEEE*, and Guo-Quan Lu, *Fellow, IEEE*

***Abstract*—Although excellent reliability has been reported for sintered silver as a die-attach material under both thermal and power cycling loads in power electronics applications, the promise of this material as a large-area attachment at temperatures beyond 200 °C needs to be investigated. This paper presents insights into the thermomechanical behavior and reliability of sintered silver under extreme thermal cycling conditions. In this study, we bonded sintered silver samples and subjected it to a thermal cycling profile of −40 °C to 200 °C with high ramp rates. We periodically monitored samples under thermal cycling to detect the presence of any failure mechanisms using a scanning acoustic microscope. We also included 95Pb5Sn solder in the study to obtain reference data. Results show the occurrence of cracks in sintered silver followed by a rapid rate of crack growth that exceeded the failure criterion in just 50 cycles. The predominant failure mechanism we observed was adhesive failure. As a large-area attachment, solder exhibited a higher reliability than sintered silver but failed within 100 cycles. Finally, we performed thermomechanical modeling to compute strain energy density values and correlated these with the experimentally observed crack growth rates to formulate a lifetime prediction model for sintered silver.**

***Index Terms*—failure mechanisms, high-lead solder, lifetime model, reliability, sintered silver, thermomechanical modeling, high-temperature power electronics.**

I. Introduction

Increased electrification of various technologies across renewable energy and energy efficiency sectors has brought a great deal of attention to power electronics components and systems to achieve cleaner and efficient modes of energy storage, conversion, and transmission [1]. The efficiency of power conversion processes heavily depends on the semiconductor die material, device topology, and related properties [2], [3]. Equally important as the device structure is the power electronics package, which can be defined as the integrated system of components surrounding the device that enable the transfer of electrical signals to and from external connections in addition to providing thermal pathways and mechanical support. A careful and meticulous design of the package including material selection, geometric layout, and integration of components—from an electrical, thermal, and mechanical standpoint—is critical to bridge the gap between theoretical and measured performance and efficiency of the devices [4]. Additionally, the package design and structure should meet the realization of system-level power electronics targets such as low cost, small footprint/volume, and high power density [5].

Depending upon the type and need of the power electronics application, wide-bandgap (e.g., silicon carbide (SiC), gallium nitride (GaN)) [6], [7] and ultrawide-bandgap (e.g., gallium oxide (Ga_2O_3), diamond) devices [8] are proving to be better candidates than traditional silicon (Si) devices due to characteristics such as higher breakdown voltage, lower switching and conduction losses, and ability to operate at higher temperatures. In electric-drive vehicles, SiC devices are now commercially available for use in the traction inverter [9], whereas GaN is preferred in DC-DC converters [10] that provide power to onboard monitoring and infotainment systems. Wide-bandgap devices are also being investigated for deployment in space, aviation, wind turbine, photovoltaic, downhole oil and gas drilling applications, among many others [11], [12]. Nevertheless, the theoretical benefits of SiC and GaN over Si devices, which is now well accepted and realized within the power electronics community, have not translated to their practical development and market penetration given the breadth and depth of challenges preventing them from reaching their full potential [13], [14]. In addition to resolving material-specific issues such as defects at the device level, the electrical-thermal-mechanical performance of the package plays a critical role in successfully attaining the promised benefits of wide-bandgap devices. Minimal parasitics, efficient heat removal, and high reliability despite the high-voltage and high-temperature operating conditions triggered by the SiC and GaN devices - while enabling system-level targets - are the desirable performance traits of an electronics package for wide-bandgap devices.

Manuscript received May xx, 2021; revised month, day, 2021; accepted month, day, 2021. Date of publication month, day, year; date of current version month, day, year. The authors acknowledge financial support for the work provided by Susan Rogers, Technology Development Manager for the Electric Drive Technologies Program, Vehicle Technologies Office, U.S. Department of Energy Office of Energy Efficiency and Renewable Energy.

P. Paret, J. Major, D. DeVoto, and S. Narumanchi are with the Center for Integrated Mobility Sciences, National Renewable Energy Laboratory, Golden, CO, 80401 USA (e-mail: Paul.Paret@nrel.gov; Joshua.Major@nrel.gov; Douglas.DeVoto@nrel.gov; Sreekant.Narumanchi@nrel.gov).

C. Ding and G.-Q. Lu are with the Bradley Department of Electrical and Computer Engineering, Virginia Polytechnic Institute and State University, Blacksburg, VA, 24060 USA (e-mail: dingchao@vt.edu; gqlu@vt.edu).

From a thermomechanical perspective, the high-temperature operation of wide-bandgap devices presents a strong materials challenge for other component layers within the package. Materials typically used in packages with Si devices such as solders cannot withstand the 200 °C and beyond operating temperature range with wide-bandgap devices, and as a result, new material formulations need to be considered [15]. It is widely documented that the failure mechanisms within a conventional power electronics package involve crack formations at the bonded interfaces (die-attach, substrate-attach) [16], along with electrical interconnect (wire bonds, ribbon bonds) failures [17]. As most of these failures are temperature-dependent, the high-temperature environment only serves to exacerbate the thermomechanical performance of these components and deserves a great deal of attention in the context of wide-bandgap devices. For the bonded interfaces, sintered silver and transient liquid phase alloys [18] are promising alternatives to solder layers because of their higher melting points and thus lower homologous temperatures, but their reliability and failure mechanisms at these extreme high temperatures are not well understood. Therefore, it is important to study the thermomechanical behavior of these materials when subjected to severe operating environments and develop lifetime prediction models. Also, it should be noted that the choice of a material as a bonded interface by an industry could depend on factors other than thermomechanical reliability, such as cost and accessibility, justifying the need for research on multiple material formulations for high-temperature power electronics packaging.

Sintered silver, as a bonded interface application, has evolved significantly in its synthesis techniques and material formulation over the past couple of decades. In the early stages of its development, the material consisted of micron-sized Ag particles or flakes, which required sintering pressure in the range of 30–40 MPa for bonding [19]. As this pressure range was considered to be detrimental to brittle ceramic substrates in the package, and to simplify and reduce the cost of fabrication, newer sintered silver solutions with nano-sized Ag particles were developed [20]. With nano-sized Ag particles, the increased surface area and corresponding enhancement in surface energy acts as the main driver of the sintering process, which then offers the possibility of lowering the required sintering pressure to almost zero. In practice, sample evaluations show that a small amount of pressure in the range of 1–5 MPa is highly beneficial in producing good-quality sintered nano-silver joints with very low void fraction [21]. A comprehensive review of the different types of commercially available sintered silver material formulations and their application methods is provided in [22].

Alongside the developments in sintered silver material formulation, there has unsurprisingly been an increased focus among researchers in conducting characterization and accelerated experiments to evaluate the shear strength and reliability of the joint. Bai and Lu [23] conducted thermal cycling from 50 °C to 250 °C of nano-silver bonded between 1.706-mm × 1.380-mm silver-metallized SiC Schottky diodes and silver- and gold-plated direct-bond-copper (DBC) substrates, where the samples survived for 4,000 and 6,000 cycles, respectively. This study considered a 50% drop in shear strength as the failure criterion. Knoerr, Kraft, and Schletz [24] performed thermal cycling (−55 °C to 175 °C, −5 °C to 175 °C) and power cycling accelerated tests on sintered nano-silver joints made with different sintering parameters and developed a lifetime prediction model using the Coffin-Manson approach. The footprint of the samples for thermal cycling was 14 mm × 14 mm and 20% growth in the crack area was considered as the failure criterion. Their results show sintered silver exhibiting a longer lifetime than solder joints such as SAC305 and 95Pb5Sn under both thermal cycling and power cycling loads. Le Henaff et. al. [25] studied the impact of various substrate metallization materials on the reliability of nano-silver die-attach joints bonded between Si diodes (3.8 mm × 3.8 mm) and transistors (6.5 mm × 4.0 mm), and large-area DBC substrates under a thermal cycling profile of −40 °C to 125 °C. Thermal resistance of the die-attach layer was monitored periodically and no changes were observed even after 2,400 cycles. Extending on these results, Le Henaff et. al. [26] formulated a lifetime prediction model with additional inputs from thermomechanical modeling. Dai et al. [27] conducted power-cycling accelerated experiments (room temperature to 165 °C–171 °C) on nano-silver and 95Pb5Sn solder die-attach layers between 13.5-mm × 13.5-mm power dies and AlN-based DBC substrates. Thermal resistance measurements of these samples report an increase of 186% from 0.047 to 0.133 K/W for the 95Pb5Sn solder after 41,000 cycles, whereas the value remained at approximately 0.04 K/W ± 0.004 K/W for nano-silver even after 116,000 cycles. Zhao et. al. [28] studied the impact of thermal aging on the shear strength of sintered nano-silver joints using 13.5-mm × 13.5-mm Si chips bonded on a bare Cu plate. In these experiments, no drop in shear strength was observed after aging the samples at 150 °C for 72 hours, but 180 °C and 250 °C temperatures resulted in a reduction of shear strength to 50% and 20% of initial values, respectively. A detailed description of various synthesis parameters that affect the shear strength of sintered silver is provided in [29] and the reviewed data point to higher reliability of sintered nano-silver joints in comparison with solder joints under similar thermal cycling profiles. Siow and Chua [30] conducted thermal cycling from −65 °C to 150 °C on both micro-silver and nano-silver bonded between 1.8-mm × 2.9-mm Si dies and Ag-plated Cu and DBC substrates and reported different failure mechanisms depending on the paste type and the substrate used.

In the past, the authors' own experiments [31] with micron-silver joints also led to proving its superior reliability over the eutectic lead-based solder under a thermal cycling profile of −40 °C to 150 °C. The sample configuration comprised a bonded material sandwiched between a 5-mm-thick Cu baseplate and DBC with Si_3N_4 ceramic, with a footprint of 50.8 mm × 50.8 mm. The sintered silver samples were bonded at Semikron [32] at a high sintering pressure of 30–40 MPa. With 20% of crack growth by area as the failure criterion, sintered silver and eutectic lead-solder joints failed at 2,300 and 1,400 cycles, respectively. In keeping with the shift in focus reported in the literature toward pressureless sintering, recent efforts at

the National Renewable Energy Laboratory (NREL) concentrated on assessing the mechanical strength and characterizing the reliability of hybrid-silver (a mixture of nano-sized Ag particles with micron-sized Ag flakes) formulations. Sintered silver samples were fabricated with coupon materials of different coefficients of thermal expansion (CTE) at Virginia Tech and subjected to a thermal cycling profile of −40 °C to 200 °C at NREL. This study includes a span of bond areas at different sintering pressures. We also performed finite element-based nonlinear thermomechanical modeling to investigate the impact of sample design features on the reliability of the sintered silver bond.

II. Experimental Approach

A. Sample Synthesis and Characterization

A common observation that can be ascertained from the literature on reliability evaluation experiments of nano-silver is its characterization as a die-attach in which the sample configuration consists of a metallic substrate bonded to either Si/SiC chips or dummy dies. In this study, the sample design comprised circular Cu and Invar disks bonded together using a hybrid silver bond. The diameter and thickness of the disks were 25.4 mm (1 inch) and 2 mm, respectively. Prior to bonding, both Cu and Invar disks were plated with approximately 5-µm-thick silver layer for solid diffusion compatibility with the silver bond and die-shear tests were conducted to evaluate the plating quality. Shear stress values greater than 30 MPa were reported, and the plating was deemed to be sufficient for sintered silver bonding. The rationale for this sample design was that the large CTE mismatch between Cu and Invar would impose mechanical stresses on the silver bond under thermal cycling, and the circular shape, without any sharp corners, limited the macroscale causes of possible failure mechanisms to just CTE mismatch and not any geometrical irregularities. Additionally, the flat outer faces of the disks offered a pathway to evaluate the bond reliability using a C-mode scanning acoustic microscope (C-SAM). A schematic of the sample design selected for this study is shown in Fig. 1.

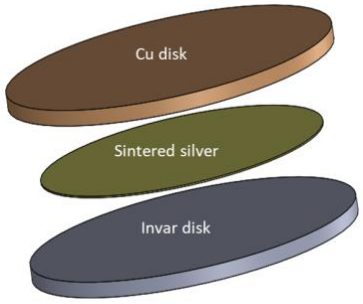

Fig. 1. Exploded view of the sample design for reliability evaluation. Both Cu and Invar disks (25.4-mm diameter, 2-mm thickness) were plated with 5-µm-thick silver before bonding with sintered silver. Samples with different bond diameter were synthesized.

The sintered silver material used in this study was purchased from NBE Tech LLC, and the sample synthesis tasks were conducted at Virginia Tech. This sintered silver formulation consists of nano-silver particles embedded within micron-sized silver flakes and has a solid loading of 89%. Multiple bonding trials with variations in the wet paste's application method and thickness were initially attempted before selecting the best synthesis profile that would result in a bond with acceptable levels of initial voiding or cracking (<5% of total bond area). These iterations included:

1) Applying the sintered silver paste on either one or both disks before joining them together and then performing the drying and sintering steps
2) Applying the sintered silver paste on both disks and completing the drying step before joining them together for sintering
3) Varying the sintering temperature.

We finally selected the second iteration, and in this synthesis process, manually printed the silver paste using a 100-µm-thick stencil on both Cu and Invar disks, and dried at 120 °C before joining them and heating the entire sample to 265 °C for sintering. We deployed thicker stencils to compensate for the nonuniformity in flatness of both Cu and Invar disks from machining. We investigated two different sintering pressure levels in this study—3 MPa and 10 MPa. In addition to the low-pressure-assisted sintering profile, we attempted a purely pressureless sintering approach, but the initial bond quality never reached acceptable levels with this method despite numerous iterations to the synthesis profile, and hence the corresponding data are not included in this paper. With each sintering profile, samples with three different bond diameters (22, 16, and 10 mm) were fabricated. Fig. 2 shows the synthesis profile employed for pressure-assisted sintered silver samples.

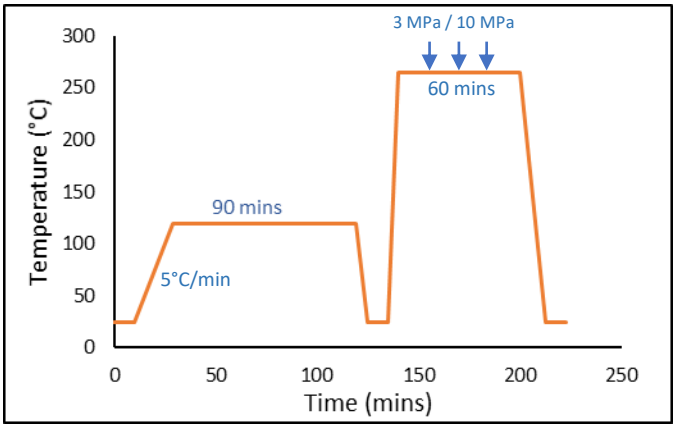

Fig. 2. Synthesis profile and bonding procedure of pressure-assisted sintered silver samples.

After sample synthesis, we imaged the sintered silver layer from both the Cu and Invar end using the C-SAM and calculated the percentage levels of cracks in these images using the Scanning Probe Image Processor (SPIP) software from Image Metrology. In addition to sintered silver, we synthesized samples with 95Pb5Sn solder as the joint to obtain reference data for comparison. Despite its high lead content, which renders it unsuitable for commercial use in the automotive industry due to policy regulations, we selected 95Pb5Sn solder purely because of its ability to operate at high temperatures and easy workability. Fig. 3 shows the bond quality of both sintered silver and solder samples after their synthesis through C-SAM

images.

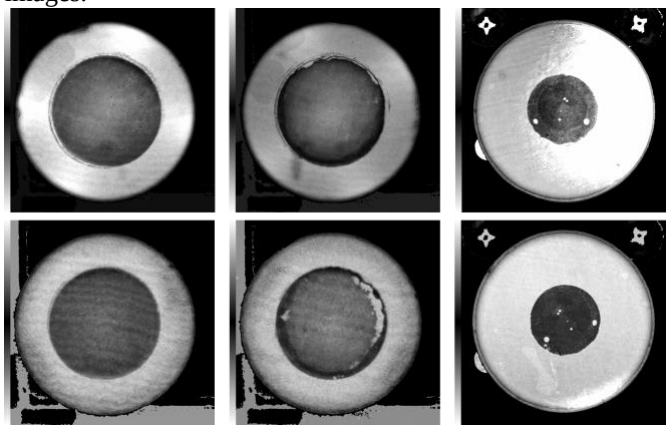

Fig. 3. C-SAM images of 3-MPa sintered silver joint (left), 10-MPa sintered silver joint (center), and 95Pb5Sn solder (right) from the Invar side (top) and the Cu side (bottom) before thermal cycling. In these images, the bond diameter of sintered silver and solder samples are 16 mm and 10 mm, respectively.

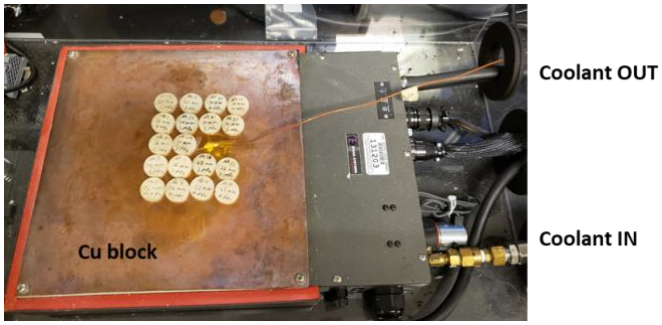

Fig. 4. Samples placed on the thermal platform for thermal cycling.

B. *Thermal Cycling*

After synthesis and initial bond quality characterization, we subjected the samples to accelerated thermal cycling under which crack initiation and propagation were expected to occur in the sintered silver joint. We used a temperature platform from Sigma Systems (inTEST Thermal Solutions), shown in Fig. 4, to conduct thermal cycling. A copper heat spreader was bolted onto the hot plate of this setup to enable uniform heat distribution and thus minimize temperature variations among the samples. Cooling was achieved by circulating liquid nitrogen through a coolant loop within the platform from a nearby cryogenic tank. We selected a thermal cycling profile of −40 °C to 200 °C for this experiment, mainly to study the impact of high-temperature effects on the thermomechanical behavior of the sintered silver. The selected profile had a very high ramp rate of greater than 25 °C/min in both directions, and the dwell time was a little over 3 minutes above 190 °C on the hot end and below −30 °C on the cold end. Overall, the total time to complete one thermal cycle was between 21–22 minutes. Fig. 5 shows the temperature versus time data logged from a sample during thermal cycling, where the blue and orange curves denote the temperature data collected via thermocouples at the bottom and top face of a sample, respectively. The samples were arranged in such a way that the Cu end of the sample was in contact with the Cu spreader of the temperature platform throughout the thermal cycling experiments.

III. THERMOMECHANICAL MODELING

Similar to the thermomechanical modeling approach in the authors' previous work [33], we conducted nonlinear finite element simulations using the ANSYS software platform to study the degradation of sintered silver under thermal cycling. We created a quarter-symmetric geometric model of the sample, as shown in Fig. 6. Only linear elastic material properties, as listed in Table I, were assigned to the Cu and Invar disks, whereas the Anand viscoplastic constitutive model was also included to simulate the thermomechanical behavior of the sintered silver joint. We obtained the Anand model parameters for sintered silver from Yu et al. [34]. By applying the Anand model in this study, we made an inherent assumption that the macroscale deformation of the sintered silver material is indeed viscoplastic in nature. Also, the microstructural evolution of the material under thermal cycling would not be captured. The minor temperature gradient within the samples at any given time during experimental thermal cycling was ignored in the simulations, and a uniform thermal cycle from −40 °C to 200 °C was applied as the load. Ramping rates between the temperature extremes and dwell times were suitably selected in the applied thermal cycle to match with the experimental data presented in Fig. 5. Symmetric boundary conditions were applied to the symmetry faces and a center node was constrained in all three directions to prevent the rigid body motion.

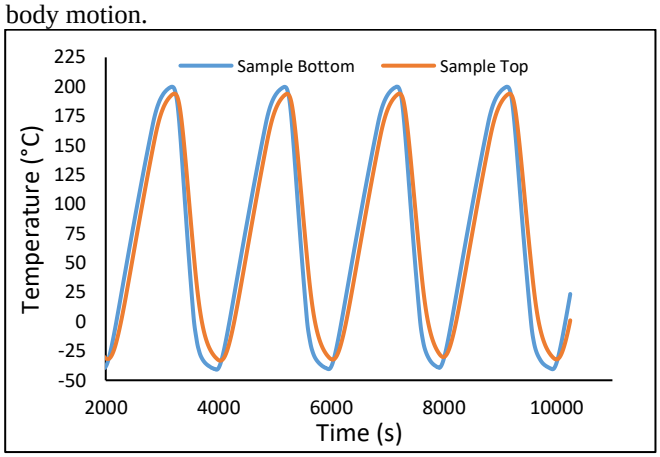

Fig. 5. Accelerated thermal cycling profile.

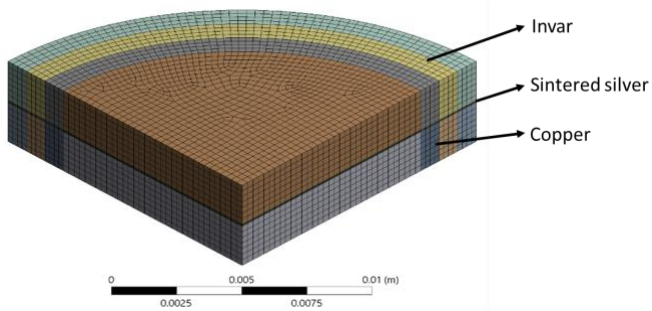

Fig. 6. Quarter-symmetric model of the sample for modeling. The geometry was sliced into different parts for ease of post-processing.

The main output of interest from these simulations is strain energy density per cycle [35] at the bond layer, a fatigue parameter used to assess the reliability of bonded interfaces. In general, a higher value of strain energy density indicates a

higher potential for failure mechanisms, which translates to a lower reliability or lifetime. Although we only considered three different bond diameters in the experimental sintered silver samples, we simulated more cases to obtain a smoother variation of strain energy density results as a function of the bond diameter. We also conducted simulations with the 95Pb5Sn solder for a comparative analysis between the two materials. The mesh was created using a mixture of SOLID186 and SOLID187 higher-order elements in ANSYS, both of which can display quadratic displacement behavior. Mesh independence of the results to within 5% was ensured in all cases. We performed all simulations on the Eagle high-performance computing cluster at NREL.

TABLE I
MATERIAL PROPERTIES AT ROOM TEMPERATURE

Material	Elastic Modulus (GPa)	Poisson's Ratio	CTE ($\times 10^{-6}$/°C)
Cu	113	0.34	16.5
Invar	141	0.3	1.3
Sintered Silver	7	0.37	20
95Pb5Sn	24	0.4	28.7

IV. RESULTS AND DISCUSSION

A. Experimental Results

1) Sintered Silver

As mentioned in section II, we fabricated samples with three bond diameters (22, 16, and 10 mm) under two sintering pressure levels (3 MPa and 10 MPa). In general, it is expected that a higher sintering pressure would drive the adhesion between the micron-sized silver flakes and the nano particles within the silver paste, thus resulting in a more compact bond. Other researchers [36], [37] have reported a reduction in porosity and an increase in shear strength of the bond at higher sintering pressures, but the porosity of the bonds was not characterized in this project as it would involve a destructive evaluation of the samples. We included a total of four samples to represent each instance, but a few of these samples displayed poor initial quality, resulting in their omission from the study. Thermal cycling was conducted up to 150 cycles with intervals at 50 and 100 cycles for C-SAM imaging.

Fig. 7 shows the C-SAM images of a couple of sintered silver samples obtained after 50 cycles. Cracking is visible as white patterns at both ends of the bond, forming toward the outer edge on the Cu side and mainly in the inner regions on the Invar side. It should be noted that this trend was observed in all samples irrespective of their sintering pressure and bond diameter, although only two sample images are presented here. Although these C-SAM images cannot reveal the chronological order of crack formations or whether a direct linkage exists between them within a sample, it is likely that the initiation and propagation of crack at one end had an indirect influence on the crack growth rate at the other end.

Fig. 8 shows the measured crack growth in all samples as a function of thermal cycles. For clarity, the figure shows measurements at only the worst-performing side, either Cu or Invar, of each sample type. The orange and blue family of curves represent samples fabricated under 3 MPa and 10 MPa sintering pressure, respectively. The 10-MPa samples with a bond diameter of 10 mm were not included, as their initial void fraction was found to be more than 10%. Overall, both sets of samples reached failure within just the first 50 cycles following the criterion of 20% crack growth by area. It could be argued that failure was reached in as few as 10 or 20 cycles, but the cycling experiments would need to be repeated with shorter cycle intervals to confirm this point. The sudden failure of these samples can be primarily attributed to the combination of high CTE mismatch within the sample structure and the external loading condition of high-temperature thermal cycling. The significant reduction in crack growth rate after 50 cycles is mainly due to the loss of stiffness in the sintered silver layer, as cracks have by then propagated across a significant length of the bond. Under both sintering pressures, samples with a bond diameter of 16 mm reported the highest mean values of crack growth, but a performance comparison between the two pressure levels or the different diameters cannot be made because the results are within the range of the standard error of these measurements, listed in Table II.

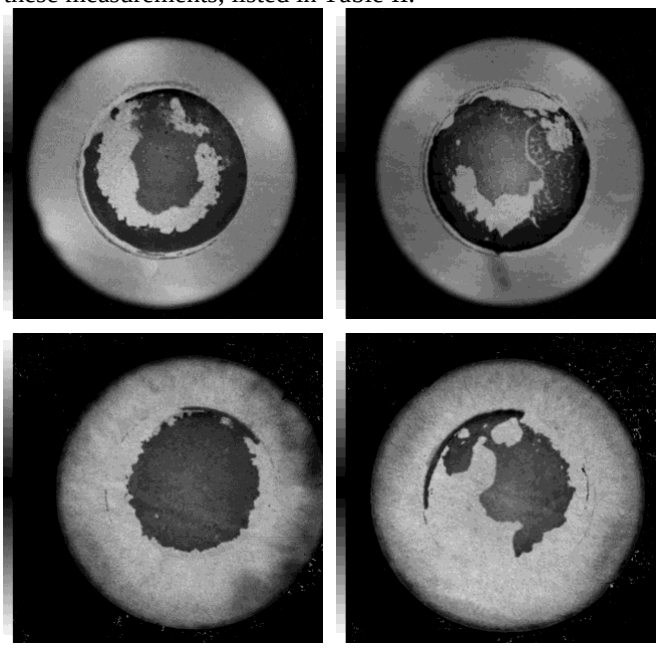

Fig. 7. C-SAM images of pressure-assisted sintered silver bonds: 3 MPa (left) and 10 MPa (right) within a sample after 50 thermal cycles from the Invar side (top) and Cu side (bottom). The white regions within the bond denote cracks or defects formed under thermal cycling. The C-SAM images of these samples before cycling is provided in Fig. 3.

2) 95Pb5Sn Solder

95Pb5Sn solder, despite being among one of the well-characterized materials in the electronics industry [38], is no longer a viable candidate for electronics packaging due to existing policy regulations that prohibit the use of lead in engineering products. As such, we chose this solder material and subjected it to thermal cycling purely to obtain reference data to compare with the reliability of sintered silver. Alternative solder candidates such as AuSn and ZnAl were either too expensive or had poor workability. In this study, we

fabricated circular samples with bond diameters of 10 mm and 25.4 mm using solder joints. Although we used solder preforms, it was challenging to maintain the joint size and shape when the bond diameter was lower than the size of outer disks due to solder reflow above the liquidus point, but the smaller the bond diameter, the easier the synthesis process was. This is also the reason for fabricating samples with 25.4-mm diameter, where the joint is flush with the outer Cu and Invar disks, as opposed to either 16- or 22-mm diameters.

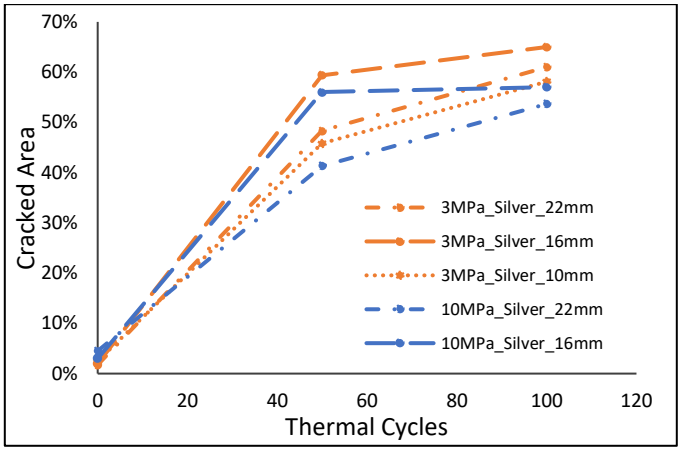

Fig. 8. Crack growth measurements in sintered silver samples.

TABLE II
STANDARD ERROR OF CRACK GROWTH MEASUREMENTS AT 50 CYCLES

Disk Thickness (mm)	Sample Type	Number of Samples	Standard Error (± %)
2	3 MPa_Silver_22mm	4	12
2	3 MPa_Silver_16mm	4	11
2	3 MPa_Silver_10mm	2	13
2	10 MPa_Silver_22mm	3	21
2	10 MPa_Silver_16mm	2	19
2	Solder_10mm	4	13
2	Solder_25.4mm	2	1
1	Solder_25.4mm	4	1

Similar to the images presented in the previous sections, Fig. 9 shows the corresponding data for the 95Pb5Sn solder. Crack formation at the bond periphery is evident in the C-SAM image from the Invar side, as indicated by the white regions within the solder joint. As opposed to the sintered silver samples, the solder samples were characterized after every 10 cycles to extract more data regarding the initial stages of crack growth. This change in cycling frequency was in fact informed by the rapid and severe degradation observed in sintered silver within the first 50 cycles of the applied thermal profile. Fig. 10 shows a comparison of the crack growth rates between solder and the 3-MPa sintered silver samples. Here, the 25.4-mm-diameter solder samples are compared with the 22-mm sintered silver samples. Although it is hard to accurately estimate the crack growth in sintered silver in the initial stages of thermal cycling due to the lower frequency of measurements, it can be observed that solder exhibited a significantly lower initial crack propagation rate in the 25.4-mm case. Also, despite the 10-mm solder samples reaching the failure criterion of 20% crack growth in just 20 cycles, the crack growth rate thereafter slows down toward the later stages of thermal cycling. Based on these experimental observations, we can conclude that under a large CTE-mismatch configuration subjected to a thermal cycling profile of −40 °C to 200 °C with high ramp rates, solder demonstrates a higher reliability potential than sintered silver for large-area attachment applications.

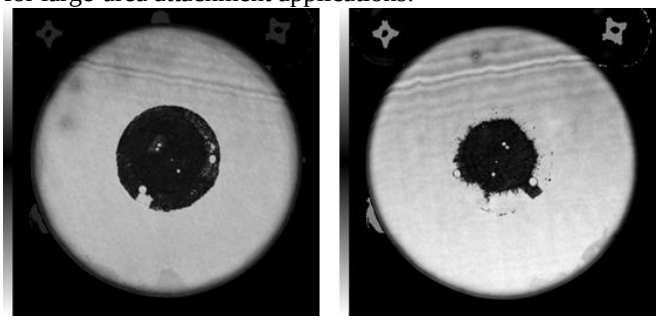

Fig. 9. C-SAM images of a 95Pb5Sn solder bond (10 mm) within a sample after 50 thermal cycles at the Invar side (left) and Cu side (right). The C-SAM images of this sample before cycling is provided in Fig. 3.

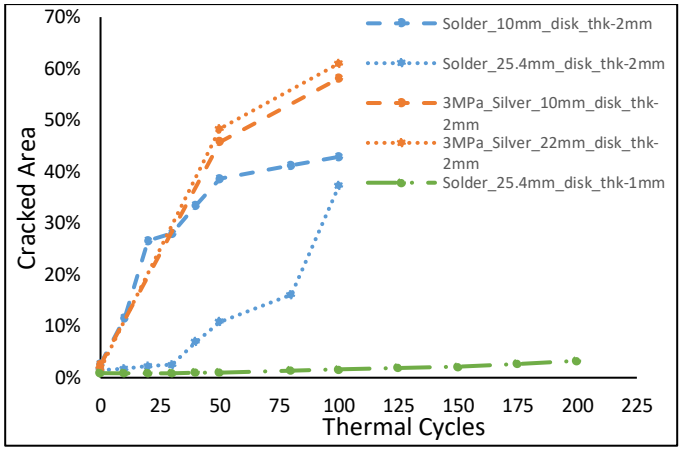

Fig. 10. Crack growth comparison between solder and sintered silver samples.

3) *Impact of Sample Thickness*

To investigate the impact of outer coupon thickness on the reliability of the bond material, we fabricated additional samples with 1-mm-thick Cu and Invar disks and subjected them to thermal cycling. In these samples, we kept the bond diameter at 25.4 mm for both sintered silver and solder joints. The objective here was to study the thermomechanical behavior of the bond materials under the same CTE-mismatch configuration but with a lower sample stiffness. Similar to the 2-mm-thick configuration, these samples were characterized using C-SAM images before the start of thermal cycling and at every 10-cycle interval. In this experiment, the initial void fraction was measured at around 2.5% and 1% for sintered silver and solder samples, respectively. Under thermal cycling, the sintered silver samples completely delaminated after just 10 cycles, whereas the amount of cracking in the solder samples was measured at around 3% even after 200 cycles, as shown by the green dash-dotted line in Fig. 10. In general, a thinner outer or adjacent disk should improve the reliability of the bond, as it allows for more compliance and a resulting reduction in the stress imparted on the joint. This trend was clearly observed for

the solder samples with their significantly lower crack growth rate, but the total delamination of sintered silver samples after just 10 cycles likely indicates a poor initial bond strength stemming from either the nonuniform flatness of the outer disks or minor variations in the synthesis process.

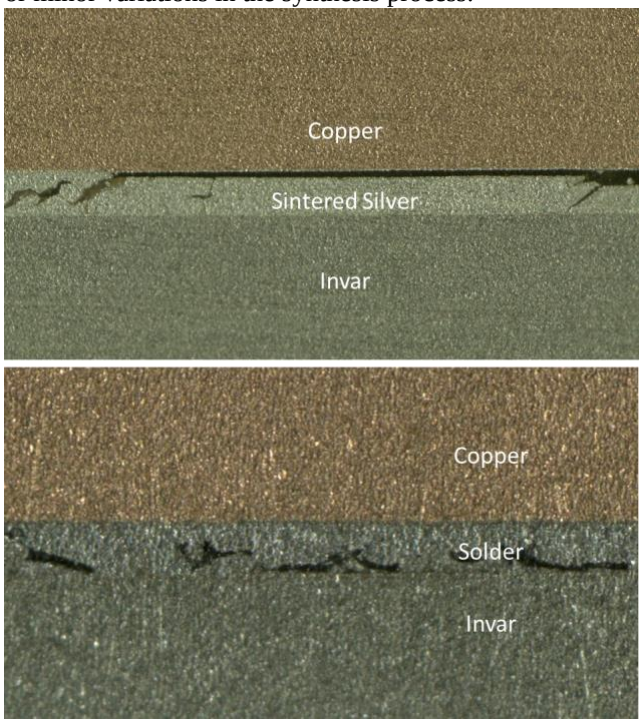

Fig. 11. Cross-sectional optical microscope images of a sintered silver (top) and a solder bond (bottom). The bond line thicknesses are approximately 140 μm and 100 μm for the silver and solder bond, respectively.

4) Failure Mechanisms

To understand the failure mechanisms that occurred in sintered silver and solder joints under thermal cycling, we obtained and analyzed cross-sectional optical microscope images of a few samples. Fig. 11 shows the cross-sectional images of a sintered silver (top) and a solder bond (bottom). In sintered silver samples, we found the overall failure mechanism to be a combination of adhesive and cohesive fracture, with adhesive fracture being predominant in general. In some cases, cohesive cracks took the form of a short, near-vertical path whereas in a few other cases, we observed extended cohesive cracking along the longitudinal direction of the bond. Cohesive cracking alone was not observed in any of the samples and in most cases, they mostly acted as a connecting path between the adhesive cracks at both interfaces. The crack likely originated in the adhesive mode at either the Cu-side or the Invar-side, and migrated to the other end through the bond, driven by the nature of pore distribution in the sintered silver material. In addition to the optical microscope images, we obtained scanning electron microscope (SEM) images of a sintered silver sample and is presented in Fig. 12. Ion milling was conducted on the cross-sectioned samples prior to the SEM imaging process. A careful analysis of SEM images reveals the presence of minor cohesive cracks between small voids within the bond region. Also, the formation of these minor cracks seems to be independent of the major adhesive cracks occurring at the interface. The bond regions between the voids could be under a larger stress concentration compared to the remaining sections, thus leading to the formation of thin cracks.

The observation of adhesive cracking in sintered silver samples in this study is similar to the results obtained by Knoerr, Kraft, and Schletz [24], but cohesive cracking was the main failure mechanism in nano-silver samples subjected to thermal cycling experiments by Siow and Chua [30]. In the case of solder bonds, a similar failure mechanism - combination of adhesive and cohesive fracture - was observed however, the crack followed a meandering trajectory initially and then extended on as an adhesive fracture. The cracks occurred mostly at and in the vicinity of the solder–Invar interface.

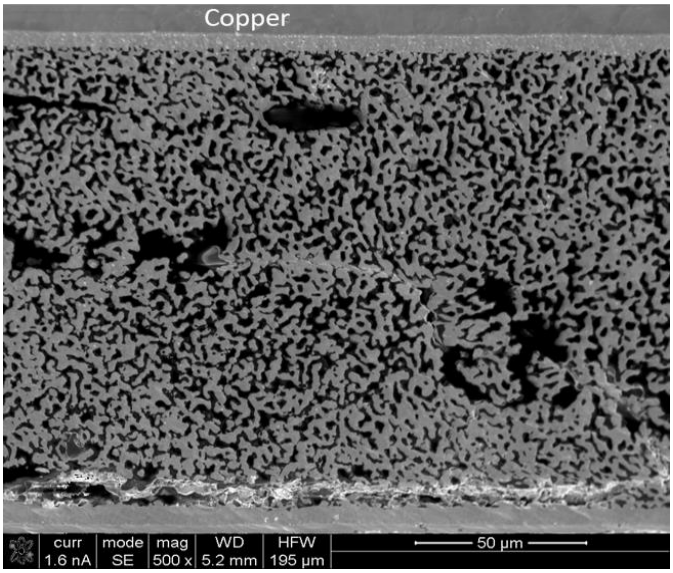

Fig. 12. SEM image of a short section of the sintered silver bond. Minor cohesive cracks between small voids can be noted.

B. Modeling Results

1) Strain Energy Density

The main objective of the finite element method-based modeling was to compute strain energy density values at the bond layer within the sample structure. Strain energy density in a mesh element within the model is the time integral of the product of stresses and strain increments over the element volume. These strain energy density values can provide insights into the deformation behavior of the bond material under various iterations of both the sample geometry and loading conditions than what were experimentally analyzed at a macroscopic level. Fig. 13 shows contour plots of strain energy density developed in the sintered silver and solder layers between Cu and Invar disks under thermal cycling. It can be observed that in both materials, the higher values of strain energy density occur at the outer regions of the bond, indicating the initiation of cracks at the periphery followed by propagation toward the inner regions—a phenomenon that was mostly observed for the experimental solder samples and on the Cu side of the sintered silver samples. Also, these values were higher in the bond region toward the interface with the Invar disk, which is due to the large local CTE mismatch between Invar and silver or solder. The nodal values of strain energy density were calculated to be higher in sintered silver than in solder, but a more appropriate metric for comparison would be

its volume-averaged value across a region of interest computed over a thermal cycle [39] than at a single load step, such as at 200 °C or −40 °C. For a given bond diameter, a 2-mm-wide annular region along the outer edge of the bond was selected in this study, and the strain energy density values computed in these regions for the different bond diameter cases are shown in Fig. 14.

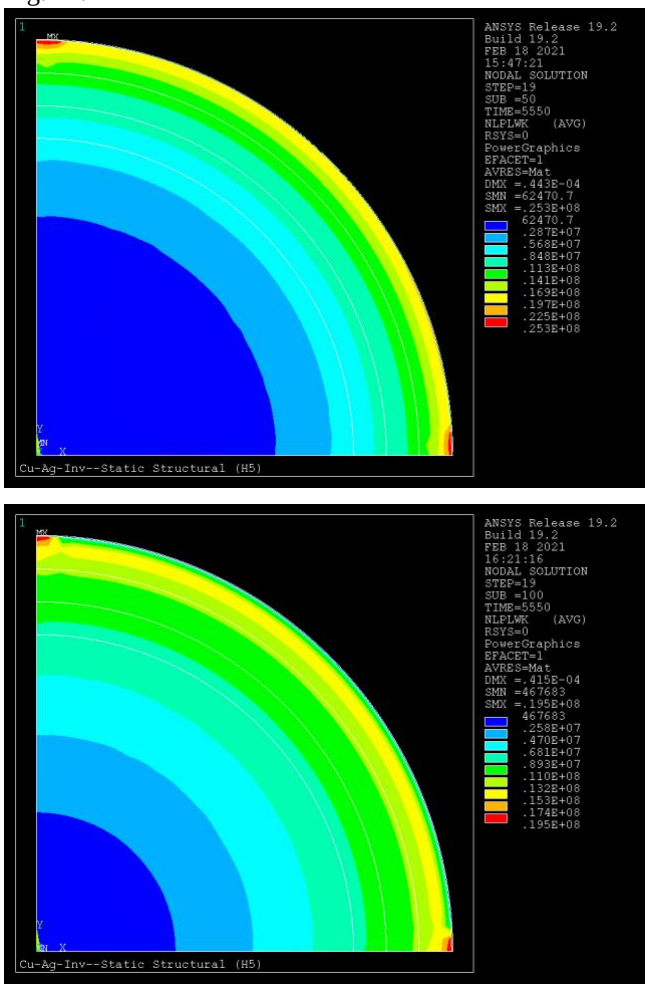

Fig. 13. Strain energy density plot of sintered silver (top) and 95Pb5Sn solder (bottom) at the 200 °C point of a thermal cycle. In these plots, Cu and Invar coupons would be below and above the bond (25.4 mm), respectively.

Both sintered silver and solder exhibit a similar trend in the variation of their strain energy density values with respect to the sample bond diameter, as shown in Fig. 14. Starting at the right end of the graph, which represents a bond diameter of 25.4 mm, strain energy density increases with decreasing bond diameter before it starts to drop. This trend is due to the difference in rate of variation of the two parameters used to compute strain energy density—strain energy and volume. Without delving into the complex patterns of stress and strain due to inelastic deformation under thermal cycling in a material, in general, a reduction in the bond diameter minimizes the induced strain energy as the total deformation is lowered. Also, because volume is an exponential function of the diameter, its rate of decrease is higher at larger bond diameters. Hence, the reduction in volume is higher for a change in bond diameter from 22 mm to 20 mm than a case such as from 12 mm to 10 mm. As a result, strain energy density shows an initial rising trend as the bond diameter is reduced due to the larger decrease in volume than strain energy. This initial increasing pattern is more pronounced in sintered silver and reaches a peak value at a bond diameter of 16 mm, which corresponds well with the experimental results where the average crack growth was observed to be the highest in 16-mm samples. Although the simulations indicate a higher rate of deformation in the 16-mm sample based on strain energy density values, readers should note that no conclusive differences were experimentally observed in the crack growth rate between samples of different bond diameters. However, modeling results of the 95Pb5Sn solder bond contradict the experimental thermal cycling results. The lower strain energy density per cycle values of the 10-mm solder samples indicate a higher reliability, but these samples had failed prior to the 25.4-mm samples. It is possible that variations between the simulation domain and the experimental samples were significant enough to cause this disagreement, but further investigation is needed to identify the root causes of failure in the solder samples.

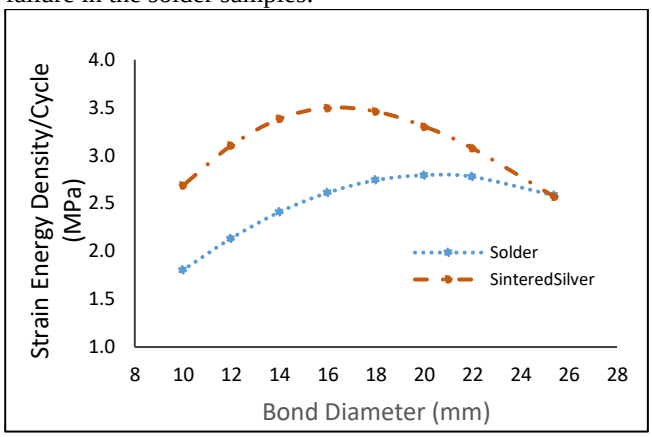

Fig. 14. Strain energy density per cycle as a function of bond diameter.

2) Lifetime Prediction Model

An agreement between the modeling and experimental results of sintered silver samples allows us to formulate a lifetime prediction model by correlating the strain energy density per cycle with the crack growth rate, as shown in Fig. 15. In this graph, the crack growth measurements of the 3-MPa sintered silver samples with different bond diameters at the 50-cycle interval were converted to crack growth rates and are expressed in percentage of the cracked area over the number of thermal cycles. We selected the 50-cycle mark because all samples were recorded to have reached the failure criterion by then. A simple power-law model, similar to a Paris' law equation, was used to define the correlation that serves as the lifetime prediction model.

From Fig. 15, the lifetime prediction model is:

$$\frac{dA}{dN} = 0.76\,\Delta W^{0.431} \qquad (1)$$

Here, $\frac{dA}{dN}$ denotes crack growth rate and ΔW represents the volume-averaged strain energy density per cycle. Although lifetime models of sintered silver exist in the literature [24], [40], the model in (1) encompasses the thermomechanical behavior of sintered silver as a large-area attachment at a high temperature of 200°C, which, to the authors' knowledge, has

not been covered prior to this study. It must be noted that this lifetime model is based on average values of crack growth rates recorded for sintered silver samples of different bond diameters, but no solid conclusions as to which bond diameter performed the best can be derived based on the experimental results alone. Also, the coefficients in the model depend on the bond region selected for volume-averaging the strain energy density results. As a 2-mm-wide outer annular region of the bond was selected in this study, practitioners of the lifetime model in (1) must be sure to select a similar geometrical region in their respective designs to obtain lifetime results with improved accuracy. Additionally, the crack growth rates obtained as outputs using (1) can be converted to cycles-to-failure predictions with failure defined as a certain percentage of crack growth by area. Apart from the typical drawbacks of an empirical approach to develop lifetime models, a restriction of the model in (1) is that it is completely based on sintered silver samples fabricated under 3 MPa of sintering pressure. Hence, application of this model to cases other than 3 MPa may result in less-accurate predictions.

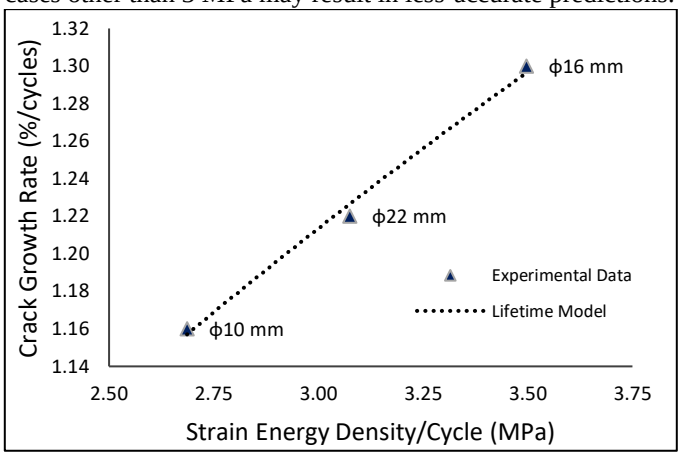

Fig. 15. Lifetime prediction model of sintered silver.

V. Conclusion

This paper presents a reliability evaluation study of sintered silver at high-temperature thermal cycling conditions. We fabricated sintered silver samples of different bond diameters in a high CTE-mismatch configuration under two different sintering pressures and subjected them to a thermal cycling load of −40 °C to 200 °C. We monitored the performance of the bond at different intervals of cycling by obtaining C-SAM images. Based on the failure criterion of 20% of crack growth by area, all sintered silver samples were considered failed in 50 thermal cycles. Reference data obtained with 95Pb5Sn solder samples reported lower crack growth rates, especially at larger bond areas. Cross-sectional microscopic images revealed the failure mechanisms to be predominantly adhesive fracture in sintered silver and a combination of adhesive and cohesive fracture in solder samples. We also computed strain energy density per cycle values of sintered silver through nonlinear finite element simulations, and correlated with crack growth rates from experiments to formulate a lifetime prediction model for sintered silver. We observed a discrepancy between the modeling and experimental results of the solder samples, and further investigation is required to identify the causes of this mismatch.

Acknowledgment

The authors would like to express sincere gratitude toward Yansong Tan for her significant contributions in fabricating sintered silver samples for this project. The authors also thank Patrick Walker and Helio Moutinho for conducting ion milling and obtaining SEM images of the sintered silver sample.

This work was authored in part by the National Renewable Energy Laboratory, operated by Alliance for Sustainable Energy, LLC, for the U.S. Department of Energy (DOE) under Contract No. DE-AC36-08GO28308. Funding provided by U.S. Department of Energy Vehicle Technologies Office. The views expressed in the article do not necessarily represent the views of the DOE or the U.S. Government. The U.S. Government retains and the publisher, by accepting the article for publication, acknowledges that the U.S. Government retains a nonexclusive, paid-up, irrevocable, worldwide license to publish or reproduce the published form of this work, or allow others to do so, for U.S. Government purposes. A portion of the research was performed using computational resources sponsored by the U.S. Department of Energy's Office of Energy Efficiency and Renewable Energy and located at the National Renewable Energy Laboratory.

References

[1] F. Blaabjerg, F. Iov, R. Teodorescu, and Z. Chen, "Power Electronics in Renewable Energy Systems," presented at the *2006 12th International Power Electronics and Motion Control Conference*, Portoroz, Slovenia, Sep. 2006, pp. 1–17, doi: 10.1109/EPEPEMC.2006.4778368.

[2] P. K. Steimer, "Enabled by high power electronics - Energy efficiency, renewables and smart grids," presented at the *2010 International Power Electronics Conference - ECCE ASIA*, Sapporo, Japan, Jun. 2010, pp. 11–15, doi: 10.1109/IPEC.2010.5542328.

[3] J. W. Kolar, F. Krismer, Y. Lobsiger, J. Muhlethaler, T. Nussbaumer, and J. Minibock, "Extreme efficiency power electronics," presented at the *2012 7th International Conference on Integrated Power Electronics Systems (CIPS)*, Nuremberg, Germany, Mar. 2012, pp. 1–22.

[4] Y. Liu and D. Kinzer, "Challenges of power electronic packaging and modeling," presented at the *2011 12th Intl. Conf. on Thermal, Mechanical & Multi-Physics Simulation and Experiments in Microelectronics and Microsystems*, Linz, Austria, Apr. 2011, p. 1/9–9/9, doi: 10.1109/ESIME.2011.5765799.

[5] U.S. DRIVE. "Electrical and Electronics Technical Team Roadmap." October 2017. [Online]. Available: https://www.energy.gov/sites/prod/files/2017/11/f39/EETT%20Roadmap%2010-27-17.pdf

[6] L. F. S. Alves *et al.*, "SIC power devices in power electronics: An overview," presented at the *2017 Brazilian Power Electronics Conference (COBEP)*, Juiz de Fora, Brazil, Nov. 2017, pp. 1–8, doi: 10.1109/COBEP.2017.8257396.

[7] K. Boutros, R. Chu, and B. Hughes, "Recent advances in GaN power electronics," in *Proceedings of the IEEE 2013 Custom Integrated Circuits Conference*, San Jose, CA, Sep. 2013, pp. 1–4, doi: 10.1109/CICC.2013.6658400.

[8] M. Higashiwaki, A. Kuramata, H. Murakami, and Y. Kumagai, "State-of-the-art technologies of gallium oxide power devices," *Journal of Physics D: Applied Physics*, vol. 50, no. 33, p. 333002, Jul. 2017, doi: 10.1088/1361-6463/aa7aff.

[9] "Benefits of SiC MOSFET in powertrain inverter for automotive applications," *Power Electronics News*, May 27, 2019. https://www.powerelectronicsnews.com/benefits-of-sic-mosfet-in-powertrain-inverter-for-automotive-applications/.

[10] J. (L.) Lu and P. Di Maso, "Electric Vehicle inverters get GaN's efficient, cost-effective values," *Power Electronics News*, Jun. 1, 2020. https://www.powerelectronicsnews.com/electric-vehicle-inverters-get-gans-efficient-cost-effective-values/.

[11] J. He, T. Zhao, X. Jing, and N. A. O. Demerdash, "Application of wide bandgap devices in renewable energy systems - Benefits and challenges," presented at the *2014 International Conference on Renewable Energy Research and Application (ICRERA)*, Milwaukee, WI, Oct. 2014, pp. 749–754, doi: 10.1109/ICRERA.2014.7016485.

[12] S. Tiwari, T. Undeland, O. M. Midtgård, and R. Nilsen, "SiC MOSFETs for Offshore Wind Applications," *Journal of Physics: Conference Series*, vol. 1104, p. 012032, Oct. 2018, doi: 10.1088/1742-6596/1104/1/012032.

[13] H. Lee, V. Smet, and R. Tummala, "A Review of SiC Power Module Packaging Technologies: Challenges, Advances, and Emerging Issues," *IEEE Journal of Emerging and Selected Topics in Power Electronics*, vol. 8, no. 1, pp. 239–255, Mar. 2020, doi: 10.1109/JESTPE.2019.2951801.

[14] C. Chen, F. Luo, and Y. Kang, "A review of SiC power module packaging: Layout, material system and integration," *CPSS Transactions on Power Electronics and Applications*, vol. 2, no. 3, pp. 170–186, Sep. 2017, doi: 10.24295/CPSSTPEA.2017.00017.

[15] R. Khazaka, L. Mendizabal, D. Henry, and R. Hanna, "Survey of High-Temperature Reliability of Power Electronics Packaging Components," *IEEE Transactions on Power Electronics*, vol. 30, no. 5, pp. 2456–2464, May 2015, doi: 10.1109/TPEL.2014.2357836.

[16] H. Ye, M. Lin, and C. Basaran, "Failure modes and FEM analysis of power electronic packaging," *Finite Elements in Analysis and Design*, vol. 38, no. 7, pp. 601–612, May 2002, doi: 10.1016/S0168-874X(01)00094-4.

[17] W. Loh, M. Corfield, H. Lu, S. Hogg, T. Tilford, and C. M. Johnson, "Wire Bond Reliability for Power Electronic Modules - Effect of Bonding Temperature," in *2007 International Conference on Thermal, Mechanical and Multi-Physics Simulation Experiments in Microelectronics and Micro-Systems. EuroSime 2007*, London, UK, Apr. 2007, pp. 1–6, doi: 10.1109/ESIME.2007.360057.

[18] G. O. Cook and C. D. Sorensen, "Overview of transient liquid phase and partial transient liquid phase bonding," *Journal of Materials Science*, vol. 46, no. 16, pp. 5305–5323, Aug. 2011, doi: 10.1007/s10853-011-5561-1.

[19] Z. Zhang and Guo-Quan Lu, "Pressure-assisted low-temperature sintering of silver paste as an alternative die-attach solution to solder reflow," *IEEE Transactions on Electronics Packaging Manufacturing*, vol. 25, no. 4, pp. 279–283, Oct. 2002, doi: 10.1109/TEPM.2002.807719.

[20] S. Magdassi, M. Grouchko, O. Berezin, and A. Kamyshny, "Triggering the Sintering of Silver Nanoparticles at Room Temperature," *ACS Nano*, vol. 4, no. 4, pp. 1943–1948, Apr. 2010, doi: 10.1021/nn901868t.

[21] P. Paret, J. Major, D. DeVoto, S. Narumanchi, Y. Tan, and G.-Q. Lu, "Mechanical Characterization Study of Sintered Silver Pastes Bonded in a Double-Lap Configuration," presented at the *ASME 2018 International Technical Conference and Exhibition on Packaging and Integration of Electronic and Photonic Microsystems*, San Francisco, CA, Aug. 2018, doi: 10.1115/IPACK2018-8276.

[22] K. S. Siow, "Are Sintered Silver Joints Ready for Use as Interconnect Material in Microelectronic Packaging?" *Journal of Electronic Materials*, vol. 43, no. 4, pp. 947–961, Apr. 2014, doi: 10.1007/s11664-013-2967-3.

[23] J. G. Bai and G.-Q. Lu, "Thermomechanical Reliability of Low-Temperature Sintered Silver Die Attached SiC Power Device Assembly," *IEEE Transactions on Device and Materials Reliability*, vol. 6, no. 3, pp. 436–441, Sep. 2006, doi: 10.1109/TDMR.2006.882196.

[24] M. Knoerr, S. Kraft, and A. Schletz, "Reliability assessment of sintered nano-silver die attachment for power semiconductors," presented at the *2010 12th Electronics Packaging Technology Conference*, Singapore, Dec. 2010, pp. 56–61, doi: 10.1109/EPTC.2010.5702605.

[25] F. Le Henaff, S. Azzopardi, J. Y. Deletage, E. Woirgard, S. Bontemps, and J. Joguet, "A preliminary study on the thermal and mechanical performances of sintered nano-scale silver die-attach technology depending on the substrate metallization," *Microelectronics Reliability*, vol. 52, no. 9, pp. 2321–2325, Sep. 2012, doi: 10.1016/j.microrel.2012.06.121.

[26] F. Le Henaff, S. Azzopardi, E. Woirgard, T. Youssef, S. Bontemps, and J. Joguet, "Lifetime Evaluation of Nanoscale Silver Sintered Power Modules for Automotive Application Based on Experiments and Finite-Element Modeling," *IEEE Transactions on Device and Materials Reliability*, vol. 15, no. 3, pp. 326–334, Sep. 2015, doi: 10.1109/TDMR.2015.2443055.

[27] J. Dai, J. Li, P. Agyakwa, M. Corfield, and C. M. Johnson, "Comparative Thermal and Structural Characterization of Sintered Nano-Silver and High-Lead Solder Die Attachments During Power Cycling," *IEEE Transactions on Device and Materials Reliability*, vol. 18, no. 2, pp. 256–265, Jun. 2018, doi: 10.1109/TDMR.2018.2825386.

[28] S.-Y. Zhao, X. Li, Y.-H. Mei, and G.-Q. Lu, "Study on high temperature bonding reliability of sintered nano-silver joint on bare copper plate," *Microelectronics Reliability*, vol. 55, no. 12, Part A, pp. 2524–2531, Dec. 2015, doi: 10.1016/j.microrel.2015.10.017.

[29] R. Khazaka, L. Mendizabal, and D. Henry, "Review on Joint Shear Strength of Nano-Silver Paste and Its Long-Term High Temperature Reliability," *Journal of Electronic Materials*, vol. 43, no. 7, pp. 2459–2466, Jul. 2014, doi: 10.1007/s11664-014-3202-6.

[30] K. S. Siow and S. T. Chua, "Thermal Cycling of Sintered Silver (Ag) Joint as Die-Attach Material," *JOM*, vol. 71, no. 9, pp. 3066–3075, Sep. 2019, doi: 10.1007/s11837-019-03461-4.

[31] P. P. Paret, D. J. DeVoto, and S. Narumanchi, "Reliability of Emerging Bonded Interface Materials for Large-Area Attachments," *IEEE Transactions on Components, Packaging and Manufacturing Technology*, vol. 6, no. 1, pp. 40–49, Jan. 2016, doi: 10.1109/TCPMT.2015.2499767.

[32] C. Göbl and J. Faltenbacher, "Low temperature sinter technology die attachment for power electronic applications," presented at the *2010 6th International Conference on Integrated Power Electronics Systems*, Nuremberg, Germany, Mar. 2010, pp. 1–5.

[33] P. P. Paret, D. J. DeVoto, and S. V. J. Narumanchi, "Thermomechanical Modeling of High-Temperature Bonded Interface Materials," in *Die-Attach Materials for High Temperature Applications in Microelectronics Packaging: Materials, Processes, Equipment, and Reliability*, K. S. Siow, Ed., Cham: Springer International Publishing, 2019, pp. 107–124.

[34] D. Yu, X. Chen, G. Chen, G. Lu, and Z. Wang, "Applying Anand model to low-temperature sintered nanoscale silver paste chip attachment," *Materials & Design*, vol. 30, no. 10, pp. 4574–4579, Dec. 2009, doi: 10.1016/j.matdes.2009.04.006.

[35] I. Guven, V. Kradinov, J. L. Tor, and E. Madenci, "Strain Energy Density Criterion for Reliability Life Prediction of Solder Joints in Electronic Packaging," *Journal of Electronic Packaging*, vol. 126, no. 3, pp. 398–405, Oct. 2004, doi: 10.1115/1.1773855.

[36] Y. Liu, H. Zhang, L. Wang, X. Fan, G. Zhang, and F. Sun, "Effect of Sintering Pressure on the Porosity and the Shear Strength of the Pressure-Assisted Silver Sintering Bonding," *IEEE Transactions on Device and Materials Reliability*, vol. 18, no. 2, pp. 240–246, Jun. 2018, doi: 10.1109/TDMR.2018.2819431.

[37] C. Chen and K. Suganuma, "Microstructure and mechanical properties of sintered Ag particles with flake and spherical shape from nano to micro size," *Materials & Design*, vol. 162, pp. 311–321, Jan. 2019, doi: 10.1016/j.matdes.2018.11.062.

[38] C. Chang, Chun-Cheng Lin, and C. R. Kao, "Fundamental study of 95 high-lead solder bump on substrates pre-soldered with eutectic PbSn," presented at the *2009 4th International Microsystems, Packaging, Assembly and Circuits Technology Conference*, Taipei, Taiwan, Oct. 2009, pp. 72–75, doi: 10.1109/IMPACT.2009.5382312.

[39] R. Darveaux, "Effect of Simulation Methodology on Solder Joint Crack Growth Correlation and Fatigue Life Prediction," *Journal of Electronic Packaging*, vol. 124, no. 3, pp. 147–154, Jul. 2002, doi: 10.1115/1.1413764.

[40] F. Le Henaff, S. Azzopardi, E. Woirgard, T. Youssef, S. Bontemps, and J. Joguet, "Lifetime Evaluation of Nanoscale Silver Sintered Power Modules for Automotive Application Based on Experiments and Finite-Element Modeling," *IEEE Transactions on Device and Materials Reliability*, vol. 15, no. 3, pp. 326–334, Sep. 2015, doi: 10.1109/TDMR.2015.2443055.